Modeling the 2003 Halloween events with EMMREM: Energetic particles, radial gradients, and coupling to MHD

K. Kozarev,[1] N. A. Schwadron,[1] M. A. Dayeh,[2] L. W. Townsend,[3] M. I. Desai,[2] and M. PourArsalan[3]

Received 15 November 2009; revised 16 August 2010; accepted 27 August 2010; published 24 November 2010.

[1] The Earth-Moon-Mars Radiation Environment Module (EMMREM) is a comprehensive numerical framework for characterizing and predicting the radiation environment of the inner heliosphere. We present a study of the October/November 2003 Halloween solar energetic particle events with an energetic particle acceleration and propagation model that is part of EMMREM, highlighting the current ability of the framework to make predictions at various locations of the inner heliosphere. We compare model predictions with Ulysses observations of protons at energies above 10 MeV in order to obtain realistic proton fluxes and calculate radial gradients for peak fluxes, event fluences, and radiation dosimetric quantities. From our study, we find that a power law with an index of −3.55 at energy of 200 MeV describes the time-integrated energetic proton fluence dependence on radial distances beyond 1 AU for the 2003 Halloween events, and an index of −4.18 is appropriate for peak proton fluxes at that energy. Calculations of radiation doses based on these simulations show average power law indices of −4.32 and −3.64 for peak dose rates and accumulated doses, respectively. In an effort to improve the predictions, we have coupled our kinetic code to results from a 3-D heliospheric magnetohydrodynamic model, WSA/Enlil. While predictions with the coupled model overall show worse agreement than simulations with steady state solar wind conditions for these large events, the capability to couple energetic particle propagation and numerical models of the solar wind is an important step in the future development of space weather modeling.

Citation: Kozarev, K., N. A. Schwadron, M. A. Dayeh, L. W. Townsend, M. I. Desai, and M. PourArsalan (2010), Modeling the 2003 Halloween events with EMMREM: Energetic particles, radial gradients, and coupling to MHD, *Space Weather*, *8*, S00E08, doi:10.1029/2009SW000550.

1. Introduction

[2] The ability to reliably predict fluxes of solar energetic particles (SEP) over periods with strong Solar activity and to calculate the related radiation doses at various locations in the heliosphere is important and very much needed for space operations. Astronaut crews and space electronics must be sufficiently and timely protected against the hazards of high fluxes of energetic electrons, protons, and heavier ions. This forecasting and warning capability is a focus of much research and model application for the various important locations near Earth, at low-Earth orbit (LEO), at the first Lagrange point (L1), and at geostationary orbits [*Reames*, 1999]. However, further effort is required for characterization of the radiation environment around the Moon, Mars, and other planetary bodies, as well as throughout the inner heliosphere [*Cucinotta et al.*, 2001]. Supporting this capability is crucial for the planned human exploration of the Moon and Mars in the coming decades.

[3] In this work we present results from our study of energetic proton propagation in the inner heliosphere (less than about 6 AU) during the most severe part of the October/November Halloween events of 2003, with a model of energetic particle propagation and acceleration, which treats the heliosphere in three dimensions, and includes the perpendicular transport of particles. Energetic particle transport models traditionally solve the focused transport equation [*Roelof*, 1969; *Kallenrode and Wibberenz*, 1997; *Ruffolo*, 1995], which considers the transport of particles only along magnetic field lines. Several recent studies include the effects of shock accel-

[1]Department of Astronomy, Boston University, Boston, Massachusetts, USA.
[2]Southwest Research Institute, San Antonio, Texas, USA.
[3]Department of Nuclear Engineering, University of Tennessee, Knoxville, Tennessee, USA.

eration by traveling interplanetary shocks as a parametric source term that is either ad hoc or is determined from shock observations [*Kallenrode and Wibberenz*, 1997; *Kallenrode*, 2001; *Aran et al.*, 2007]. Finally, there have been modeling efforts to combine self-consistently the microphysics of diffusive shock acceleration with particle propagation [*Verkhoglyadova et al.*, 2008]. In these studies, only the parallel transport of particles to field lines has been studied. In a recent parametric study, *Zhang et al.* [2009] have modeled the propagation of solar energetic particles in three dimensions, also taking into account their transport perpendicular to magnetic field lines, solving the focused transport equation using stochastic methods. Their method requires running multiple simulations to obtain values for the particle distribution function at different positions, momenta, and pitch angles. Furthermore, studies of particle transport tend to focus on the transport and acceleration of energetic particles from the Sun to near Earth.

[4] As part of the EMMREM framework [*Schwadron et al.*, 2010], we have developed a model for solar energetic particle propagation and acceleration, which is geared toward space weather applications. Similarly to the model of *Zhang et al.* [2009], it treats perpendicular particle transport, and is capable of taking into account the differences in particle fluxes injected at different longitudes and latitudes, but it solves for particle fluxes at multiple locations in the inner heliosphere within a single simulation. The model is fully integrated in the framework as a tool solving for the transport of solar energetic particles accelerated in coronal shocks and released onto the three-dimensional interplanetary magnetic field. The proton fluxes at the various locations of interest are then used as an input to another model, which calculates particle radiation dose rates. Because we are interested in the realistic distribution of energetic particles near Earth and further out during solar events, and due to the scarcity of observational particle data within 1 AU, the particle propagation model Energetic Particle Radiation Environment Module (EPREM) currently has an inner boundary close to Earth, and can be configured to extend out to arbitrary distances from the Sun. We describe briefly the EPREM model in section 2.

[5] We present results from our study of SEP propagation in the inner heliosphere during a period from the October/November Halloween SEP events of 2003. We have chosen the Halloween events for several reasons: (1) they are well studied and represent a sequence of large, complex events that could pose serious radiation hazards to space operations; (2) these events were observed by multiple spacecraft throughout the heliosphere; (3) the longitudinal positions of Earth, the Moon, Mars, and Ulysses during the SEP events afford the possibility for direct magnetic connectivity along the large-scale interplanetary magnetic field to be established; and (4) the interplanetary environment over large radial and longitudinal extent was affected, as evident from observations. While the results of this study are preliminary, we hope they are a step toward more realistic modeling of energetic particle fluxes, and prediction of radiation dose enhancements due to solar eruptions in the inner heliosphere. In section 3 we summarize briefly the interplanetary conditions during the Halloween events of 2003 based on previous studies of spacecraft observations. In section 4 we present the results of our simulations. We have attempted to match the 5 AU observations with our model for energies relevant for energetic particle radiation, in order to compute radial gradients of dose rates in the inner heliosphere for these extreme events.

[6] Knowledge of the large-scale interplanetary magnetic field configuration and the solar wind properties is crucial for determining the SEP fluxes at different locations in a three-dimensional heliosphere. The EPREM model in its current state uses a simple time-independent description for the solar wind properties, a constant solar wind, Parker spiral magnetic field, and density scaling with the inverse square of radial distance. In an effort to improve the predictions of the three-dimensional transport of solar energetic particles, we have developed an interface to include simulation results from the Enlil heliospheric numerical magnetohydrodynamic (MHD) model [*Odstrcil*, 2003] in our particle calculations. This model is widely used in the heliophysics community for studying solar wind conditions in the inner heliosphere [*Webb et al.*, 2009; *Baker et al.*, 2009]. In section 5 we compare particle fluxes calculated by using this coupled mode (hereafter EPREM+Enlil simulation) with the version utilizing a time-independent analytical Parker spiral solar wind (hereafter EPREM simulation). We summarize our study in section 6.

2. Energetic Particle Radiation Environment Module Model

2.1. EPREM Description

[7] The Energetic Particle Radiation Environment Module (EPREM) is the backbone of the EMMREM framework. It is a parallelized energetic particle transport and acceleration numerical kinetic code, solving for energetic charged particle distributions in the three-dimensional heliosphere. The model includes the effects of pitch angle scattering, adiabatic focusing and cooling, convection and streaming, and stochastic acceleration. The solver requires inner boundary conditions, with no initial conditions imposed. We have developed a dynamical simulation grid, in which the computational nodes are carried away from the Sun (frozen in) with the solar wind; thus, the connected grid nodes (streamlines) naturally assume the shape of a three-dimensional interplanetary magnetic field, along which energetic particles propagate. The modular design of EPREM allows for the model of interplanetary magnetic field to be changed easily. In its original formulation, EPREM uses a model with a radial field component falling off as the inverse square of radial distance, azimuthal component falling off as the inverse of radial distance, and a constant latitudinal component (the

so-called Parker spiral). The spatial grid is housed in a data structure based on nested cubes, whose surfaces are regularly subdivided into square arrays of square cells. These cells represent the structure of the grid, within which computational nodes propagate. The inner boundary surface rotates with the solar rotation rate, and is expelled outward at the solar wind speed. At each time step, a new shell of cells is created at the inner boundary of the grid, and starts its propagation outward.

[8] The advantage of such a grid is that computations are done in the frame moving with the solar wind, allowing to readily solve a form of the focused transport equation [*Kóta et al.*, 2005], in which most state quantities (e.g., density, field strength, plasma velocity) are cast as time derivatives. *Schwadron et al.* [2010] present a full description of the governing equation and its terms. EPREM has been designed to incorporate perpendicular transport of particles, and includes a solver for cross-field diffusion and particle drifts. Appendix A describes the numerical technique we use for computing the contribution of cross-field diffusion to particle transport. The code can be modified to work in various energy regimes, from keV to GeV. EPREM is capable of solving for the transport of multiple energetic particle species, and it produces time histories of the distribution functions at various pitch angles, energies, and locations in the heliosphere. To obtain high-precision three-dimensional positions of bodies of interest in the heliosphere (solar system bodies, spacecraft, and other relevant locations), we have developed an interface to the SPICE toolkit (http://naif.jpl.nasa.gov/naif/aboutspice.html), created and maintained by NASA's Navigation and Ancillary Information Facility. The time-dependent distribution function values for a spectrum of energies and pitch angles are recorded for multiple species at desired locations within the heliosphere, which we will call "observers" in the rest of the paper.

[9] The inner and outer radial boundaries of the EPREM model, spatial and temporal resolution, energy range and resolution can all be altered easily by modifying appropriate configuration files, without the need to modify the actual code. This adds to the flexibility of the model to be applied to various astrophysical domains, for example simulating energetic particle transport in other stellar systems. For the purpose of characterizing time-dependent energetic particle radiation in the inner heliosphere caused by real SEP events, we have chosen to use 1 AU as the inner boundary of the EPREM computational grid, since a wealth of in situ observations of SEPs exist near Earth, which the model can use as inner boundary conditions. In particular, we have made an interface to energetic proton observations from the GOES fleet of satellites, and made them the standard source of data input to the model, since the GOES data set covers solar cycles 22 and 23 and delivers proton fluxes over a broad energy range. In the future, we plan to include a model of particle acceleration by shocks, and extend the inner boundary to within a fraction of an AU from the Sun.

[10] When modeling energetic particle propagation and acceleration in the heliosphere, care must be taken to include correct information about the interplanetary field and the connectivity between Earth and the sources of SEPs, the presence of long-lived structures (such as CIRs), and whether there are coronal mass ejections (CMEs) and particle-accelerating interplanetary shocks associated with them. By using real heliospheric positions in our simulations, we make sure to include appropriate longitudinal connectivity between SEP sources and observers. Furthermore, corotating interaction regions (CIRs) and associated shocks are usually not efficient in accelerating charged particles to high-enough energies (usually up to 10 MeV/nuc), such that can pose significant radiation hazards [*Mason et al.*, 1999; *Wilson et al.*, 1991]. However, they can alter the large-scale pattern of magnetic connectivity, thus influencing the interplanetary particle propagation [*Wilson et al.*, 1991], and thus are important to include in modeling particle transport. We have attempted to do this by including numerical MHD model results of the quiet time solar wind for the period of the Halloween events.

[11] Last, in this work we do not model the contribution to particle acceleration of traveling interplanetary CME-associated shocks that survive beyond 1 AU. Instead, we essentially model the propagation of high-energy ($E >$ 10 MeV) protons that have been accelerated by CME-driven traveling shocks between the Sun and 1 AU and released near Earth onto a Parker spiral magnetic field lines. There is a growing body of theoretical and observational work, suggesting that in many SEP events driven by traveling CME-associated shocks, most of the particle acceleration occurs early in the events, when the shocks are closer to the Sun than to Earth. *Ruzmaikin et al.* [2005] evaluate the radial dependence of peak fluxes of protons accelerated by traveling interplanetary shocks between the Sun and 1.4 AU using self-consistent simulations of shock acceleration and particle propagation. These authors conclude that the maximum fluxes decrease with radial distance according to a power law, with the power index varying with energy between –2.3 and –3 for energies between 1.0 and 100.0 MeV. This softening of the shock-accelerated proton spectra with radial distance has also been documented in observations [*Kallenrode et al.*, 1993]. *Kocharov et al.* [2009] examine a major event from cycle 23, for which particle fluxes peaked much before the shock had reached Earth (where observations were made). They associated the particle profiles with acceleration by coronal shocks and later by decelerating interplanetary shocks. *Neal et al.* [2008] have shown that for many major SEP events, peak intensities of high-energy protons associated with high radiation dose rates were observed when the particle-accelerating shocks were closer to the Sun rather than to Earth, suggesting that interplanetary shocks may become inefficient accelerators for charged particles with increased radial distance, at high-enough energies connected with radiation damage (above 30 MeV/nuc). Nevertheless, interplanetary traveling sources are important for space weather applications near Earth. As mentioned

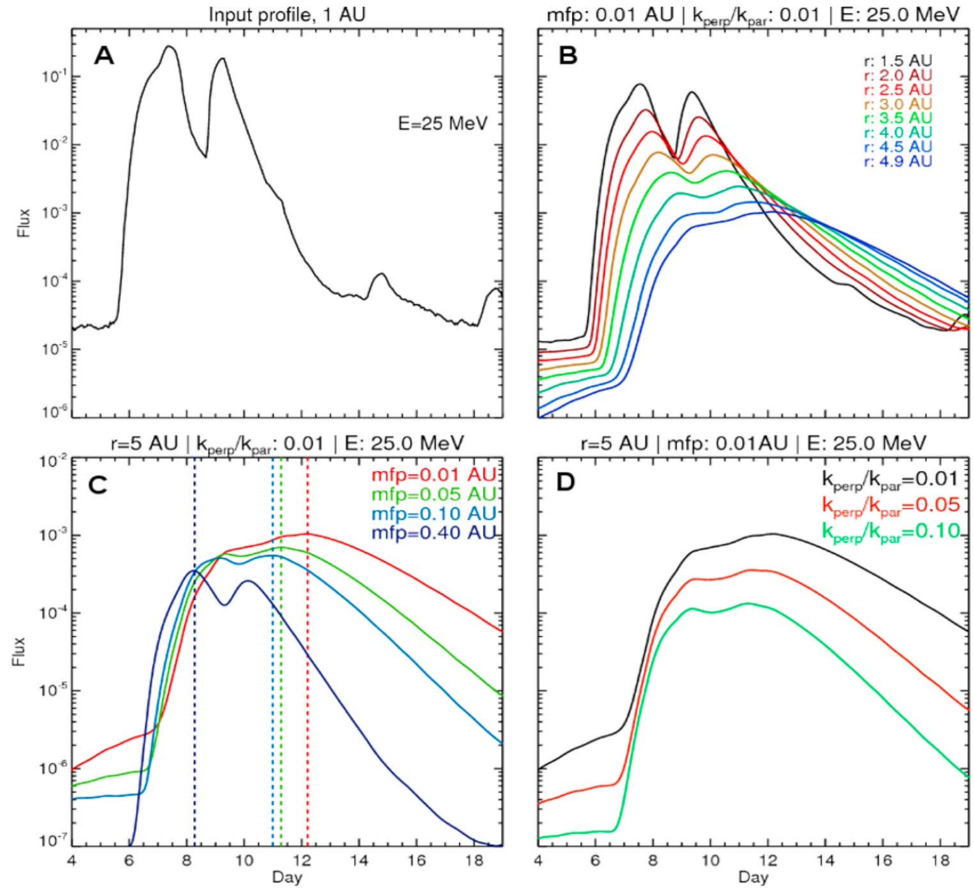

Figure 1. Some properties of the EPREM model as deduced from a series of simulations. (a) Proton flux time series for an energy of 25 MeV at the inner boundary/source region of the model, 1 AU. (b) Modeled proton fluxes at different radial distances from the Sun between 1.5 and 4.9 AU, at 25 MeV proton energy. This simulation was run using a scattering mean free path of 0.01 AU and a ratio of perpendicular to parallel transport of 1%. (c) Several simulated profiles for 25 MeV protons at 5 AU are overplotted to highlight the effect of varying the parallel mean free path in the model. Vertical dashed lines denote the positions in time of the peak flux values. (d) A comparison of simulated profiles at 25 MeV energy at 5 AU for different values of perpendicular to parallel transport ratio.

before, we plan to include the contribution of traveling shock-accelerated energetic particles in future work.

2.2. EPREM Verification

[12] A considerable amount of work has been done to determine values of the mean free path and amount of perpendicular diffusion for energetic particle transport in the inner heliosphere. Observationally, values of the parallel scattering mean free path lie between 0.08 and 0.3 AU for keV to GeV energies, and may increase with increasing particle rigidity [*Giacalone*, 1998]. However, the dependence on rigidity is still under debate, and so we have not considered it in our simulations. In terms of modeling efforts, *Zhang et al.* [2009] use radial mean free paths of 0.05 and 0.2 AU at 100 MeV, which correspond to 0.025 and 0.1 AU parallel mean free paths in the vicinity of the Earth (Parker spiral angle of 45°). *Zank et al.* [2000], among others, employ a parallel mean free path that is dependent on both the particle energy and the distance from the Sun. However, *Dröge* [2000] points out that the radial dependence of the mean free path varies considerably from one event to another. We do not currently have a way to constrain that dependence, so we have chosen a simpler approach for this study, using a constant parallel mean free path that does not change with rigidity or radial distance. For the simulations presented here, we have varied the mean free path between 0.01 and 0.5 AU. The ratio of perpendicular to parallel diffusion can also vary considerably between events, and is usually reported between 0.01 and 0.1 [*Giacalone*, 1998]. However, *Dwyer et al.* [1997] report order-of-unity ratios for particle transport in CIRs. The dependence of perpendicular transport on rigidity is unclear, with some authors

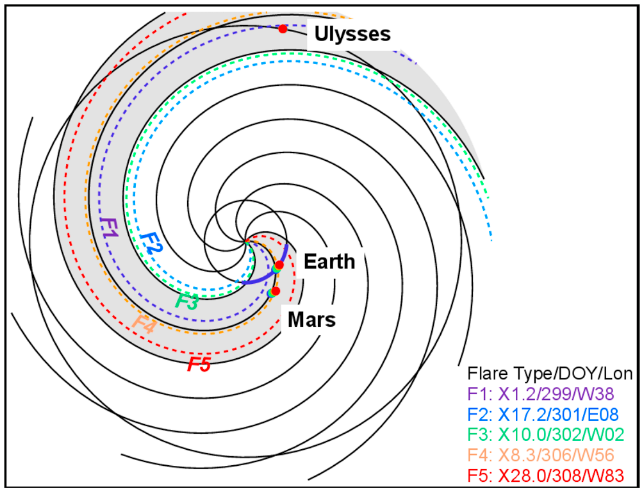

Figure 2. An equatorial plane sketch of the inner heliosphere is shown for the October/November 2003 events. The black lines trace a nominal Archimedean spiral magnetic field. An average value of the solar wind speed of 480 km/s has been chosen for this period. The dashed spiral lines denote the Sun-connected field lines corresponding to the locations of the five biggest flares that erupted during the events period, and their classes, times, and heliographic longitudes are shown in the legend at the bottom right. The positions of Earth, Mars, and Ulysses at the time of each flare are marked by solid circles corresponding in color to the flares. The shaded gray area bounded by red spiral arms covers a longitude of 80°, centered at the time of the first flare (DOY 299) on Earth's position, the orbit of which has been sketched with a circle. The purple arc at the radial distance of Earth denotes the longitudinal extent of the energetic particle source used in the EPREM model.

reporting little dependence [*Giacalone*, 1998]. In this work, we assume perpendicular to parallel ratios independent of rigidity or magnetic field strength.

[13] We present here some verification of EPREM's performance. Figure 1 shows the results of a verification study of the EPREM model. We have used a two-peak profile of protons observed at Earth, as the inner boundary of the model at 1 AU, seen in Figure 1a. Figure 1b shows a comparison of the results from a particular run as a function of radial distance from the Sun. We have assumed a Parker spiral magnetic field, a constant scattering mean free path of 0.01 AU, and 1 percent perpendicular transport for this simulation. We have collected energetic proton flux output from eight different locations between 1.5 and 5 AU, at intervals of 0.5 AU. All the observers are located along a spiral path consistent with the solar wind speed. The simulation includes both parallel and perpendicular transport effects. Several effects of the particle propagation can be observed at different radial distances: (1) peak proton fluxes diminish with radial distance; (2) flux profiles become smoothed out in time, so close to 5 AU the two peaks of the time series at 1 AU are no longer discernible; (3) protons take longer to reach observers at farther distances; and (4) proton fluxes take longer to decay after they have reached a peak. These effects are observed in spacecraft data, and they are due to a combination of all transport terms that are considered in the focused transport equation and perpendicular transport.

[14] In Figure 1c we have compared the output of EPREM at a single location (5 AU) for four simulations. The only difference in the setup of these runs is the value of the scattering mean free path: it varies between 0.01 AU and 0.4 AU. This comparison illustrates the effect of parallel transport of protons. Particles with longer mean free paths do not interact as much with local fields, and travel faster along field lines. As can be seen in Figure 1c, they reach the location of the observer faster than particles with smaller scattering mean free paths. Protons with larger mean free paths also tend to reach their peak fluxes before protons with smaller mean free paths (denoted by vertical dashed lines), but exhibit lower peaks. Another effect can be seen in the profile with mean free path of 0.4 AU (dark blue); the signature of the double peak is still visible in this time series, signifying the reduced amount of diffusion. Again, the proton fluxes for the shorter mean free paths take longer time to decay after the peak.

[15] Finally, Figure 1d shows a similar comparison to Figure 1c, but instead of varying the scattering mean free path, we have varied the fraction of perpendicular diffusion to the magnetic field lines protons experience, between one and ten percent. The main effect that can be seen is that of reduced fluxes throughout the time series. The reason for this reduction is that particles tend to spread onto other field lines and the observer does not see an increasing fraction of them as the amount of perpendicular diffusion increases. The other effect that can be seen is narrowing of the profiles in time with increasing perpendicular diffusion.

3. Energetic Particle Observations at Earth and Ulysses

[16] During the period 21 October to 12 November 2003, Earth and Ulysses were separated by about 120° in longitude, but were both within 6° from the plane of the ecliptic. Figure 2 shows a polar plot of the inner heliosphere out to 6 AU with the positions of Earth, Mars, and Ulysses (the Moon is too close to Earth to plot on this scale), and nominal Parker spiral magnetic field lines, showing the gross orientation of the interplanetary magnetic field assuming a solar wind speed of 480 km/s, which was the average measured at 1 AU during this period. The inner and outer circles denote the heliocentric distance of Earth and Ulysses at the start of the events. The gray region covers a longitudinal range of 80° around the Earth-connected field line. Finally, the dashed spiral lines show the nominal interplanetary field lines connected to

Table 1. Solar Flares From 26 October to 12 November 2003 Based on Tables of *Lario et al.* [2005]

Date	X-ray Onset	Class	Hα Location	NOAA AR
26 Oct	299/1721	X1.2/1N	N02W38	0484
28 Oct	301/1100	X17.2/4B	S16E08	0486
29 Oct	302/2037	X10.0/2B	S15W02	0486
2 Nov	306/1703	X8.3/2B	S14W56	0486
4 Nov	308/1929	X28/3B	S19W83	0486

the longitudes on the Sun of the five strongest flares during the period of activity (listed in Table 1).

[17] The October/November 2003 series of events occurred in the declining phase of the solar cycle 23 [*Dryer et al.*, 2004], after a 2 month long period of minimal activity on the Sun. We show in Figures 3 and 4 particle fluxes observed within the period of interest in this paper, 25 October (DOY 298) 2003 to 12 November (DOY 316) 2003, with the Geostationary Operational Environmental Satellite 11 (GOES 11) and Ulysses spacecraft, respectively.

[18] The energetic particle observations at 1 AU reveal the complex nature of the series of solar events that took place in October and November 2003 and their footprint on the heliosphere. Data obtained from the Energetic Particle Sensor (EPS) instrument [*Sauer*, 1993] on the GOES 11 satellite show multiple enhancements in the proton fluxes over the duration of the events (see Figure 3). Some of these abrupt flux enhancements (DOY 299, 301, 308) are cotemporal in all energy channels, signifying the arrival of

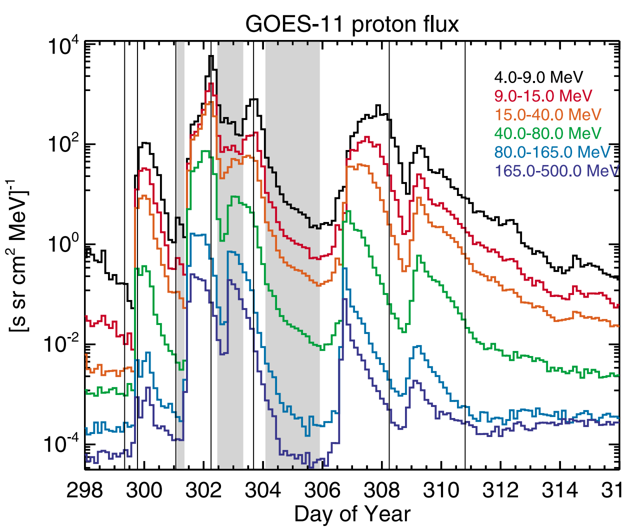

Figure 3. The 2003 particle events were very complex, with multiple flares, CMEs (gray-shaded regions), and interplanetary shocks (vertical solid lines). Shown are the multiple proton flux enhancements recorded at Earth in the energy range 4.0–500.0 MeV. Energetic particle flux time histories near 1 AU observed by the GOES 11 satellite's EPS instrument show evidence of many different events giving rise to a complex time history with potentially hazardous events. These time series were used to drive the EPREM model.

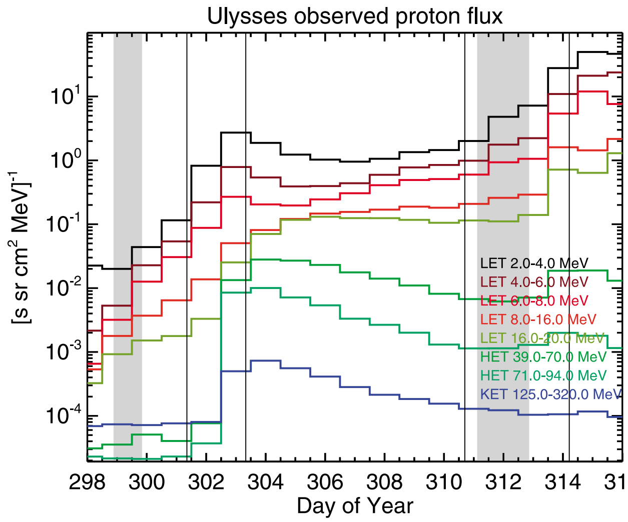

Figure 4. Energetic particle flux time histories observed by the Ulysses satellite's COSPIN suite of instruments [*Simpson et al.*, 1992] showed a completely different picture than what was observed at 1 AU. At approximately 5.2 AU from the Sun during the events, Ulysses observations show no sign of the multiple abrupt enhancements recorded in comparable energies near Earth. Instead, there are two large enhancements seen in proton fluxes between 2.0 and 320.0 MeV, peaking around DOY 303 and around DOY 314. Only the first one was observed at Earth. CME passages are denoted as gray-shaded regions, and interplanetary shocks are denoted as vertical solid lines.

IP shocks or possible sudden establishment of magnetic connections to the Sun; some of them display velocity dispersion characteristic of arrival of protons accelerated near the Sun (DOY 302–303, 306–307). Energetic protons near Earth did not respond to the passages of corotating interaction regions, or CIRs. However, *Lario et al.* [2005] suggested that CIRs may have played a big role in building the observed time profiles further out in the heliosphere, e.g., at Ulysses, not via CIR-driven shocks accelerating particles, but through changing the large-scale interplanetary magnetic field topology and thus altering the passage of energetic particles.

[19] *McKibben et al.* [2005] analyzed the interplanetary conditions at 5.2 AU during the October/November 2003 SEP events by studying Ulysses observations of energetic particles, magnetic field, solar wind speed and density, and relativistic electron observations, in order to determine the sources and propagation of the observed energetic protons. Shown in Figure 4 are daily pulse height analysis (PHA) proton fluxes from the COSPIN/LET/HET/KET instruments [*Simpson et al.*, 1992]. Differential fluxes at various energies are shown in different colors. An interesting feature in the flux profiles is the gradual increase of the SEP fluxes at energies less than 20 MeV starting on DOY 298, which is absent from the fluxes

observed at higher energies. According to *Lario et al.* [2005], this may be due to particles from eastern solar events that occurred in the days before the major Halloween events, diffusing slowly in the heliosphere. Further increases in fluxes, and especially the abrupt jump in fluxes at the four lower-energy channels shown in Figure 4 on 28 October (DOY 301) have been associated with a sudden change in connectivity between Ulysses and the Sun due to a stream interface within the CIR passing by the spacecraft [*Lario et al.*, 2005]. Those increases happened too early to be temporally related to the big X-class flare on DOY 301 and to the associated SEP injection, but were instead attributed to protons from an older event. Further proton jumps at energies >39 MeV were not observed until DOY 312, possibly because of the soft spectra of the parent solar events.

[20] The next big increase of energetic proton fluxes was observed by Ulysses on 8 November (DOY 312) in all COSPIN energy channels. It was attributed by *Lario et al.* [2005] to two fast backside halo CMEs that left the Sun on 6 and 7 November. These CMEs were only observed by the LASCO coronagraph on the Solar and Heliospheric Observatory (SOHO) at L1, but not in situ near Earth. These authors further suggested that the observed flux onset was possibly affected by an ICME interacting with a CIR, both of which crossed the spacecraft between 7 and 9 November. To partially constrain the expectations of agreement between the Ulysses observations and the EPREM model, we should mention here that we do not expect the model to reproduce the time profiles of this secondary increase of proton fluxes on 8 November.

[21] The observed profile seems to have been governed by the specific magnetic connectivity between the spacecraft and a complex stream interaction structure, combined with a moving source of energetic particles that departed the Sun on the opposite side from the Earth (and was not observed in situ at 1 AU), which our model with an analytic time-independent specification of the solar wind parameters does not include. Furthermore, the model's inner boundary conditions are determined from 1 AU observations near the longitude of Earth, and so the associated particle flux increases would not be transported to the inner heliosphere beyond Earth. However, we do expect to observe enhancements in the modeled proton fluxes based on the time-dependent description of the heliospheric solar wind plasma density, velocity and magnetic fields from the inclusion of global MHD modeling results, for long-lived structures. In particular, corotating plasma streams are present in the Enlil solution for the solar wind, so we hope to see changes in the particle fluxes related to the passages of those streams through the heliosphere.

4. Modeling the Halloween Events With EPREM

4.1. Model Parameters and Simulation Setup

[22] The simulations discussed below were performed in a parallel fashion on an 8-processor computer at Boston University. They were run using energetic proton data between DOY 294 and DOY 316 of 2003 from GOES 11 spacecraft's EPS instrument as time-dependent inner boundary conditions. Even though the GOES 11 spacecraft is within the Earth's magnetosphere, the energetic proton observations during these events show agreement between lower- and higher-energy channels (see Figure 3), and thus protons during these events belong overwhelmingly to the solar source. In addition, we have excluded the lowest-energy proton channel data as it is usually contaminated by terrestrial protons (E < 5 MeV/nuc). The computational grid was configured with cell dimensions of 0.07 AU by 6° by 8.6°, on average. At the resolution used, the simulations took around 2.5 days of real time for 25.5 days of data input, or approximately ten times faster than real time. As explained by *Schwadron et al.* [2010], the energetic particle solver is broken into several steps corresponding to solving for the different energetic particle transport effects at each node. Each of those steps has a characteristic time step, which is a fraction of the macro time step, and is determined self-consistently by the code to insure numerical stability. Usually, the smallest sub time steps are determined by the particle diffusive streaming at the highest energies in the simulation. The EPREM computational domain consists of dynamic nodes convecting radially outward with the constant solar wind speed and rotating at the solar rate, forming a Parker spiral pattern. We have used an average constant solar wind speed of 480 km/s in order to propagate the simulation grid nodes in the EPREM simulation. The particle distribution function, plasma parameters, as well as any gradients in these quantities are computed on this dynamical grid. The radial domain of the simulation spans between 0.99 AU and 6.0 AU. For the underlying plasma environment, we have used $|B_0|$ = 5 nT and n_0 = 5 cm^{-3} at 1 AU.

[23] Of the five major SEP events we consider at Earth, four have been associated with halo CMEs directed at Earth [see *Lario et al.*, 2005, Table 2]. The CME on DOY 299 was determined to be at least 170° wide. Thus, the shocks those CMEs drove were most likely directed away from Ulysses, and the large-scale spiral field lines nominally connected to the vicinity of Ulysses throughout the studied period may have interacted with the eastern flanks of these CME-driven shocks for most of this period. *Cane et al.* [1988] deduce 60° as a mean longitudinal expansion of shock drivers (CMEs), but suggests that the shocks themselves can extend much more in longitude, effectively spreading energetic particle fluxes to field lines over vast longitudinal ranges, sometimes more than 180°. The longitudinal range over which the energetic particle source is effective can be modified in EPREM, and can be considered a parameter of the model. In this study, we have chosen a source width of 80°, centered on Earth, which in our opinion is acceptable, given that all five major CMEs were halo-like as observed from Earth (see Figure 2). This assumption will have to be refined in the future through further studies of the angular extent of

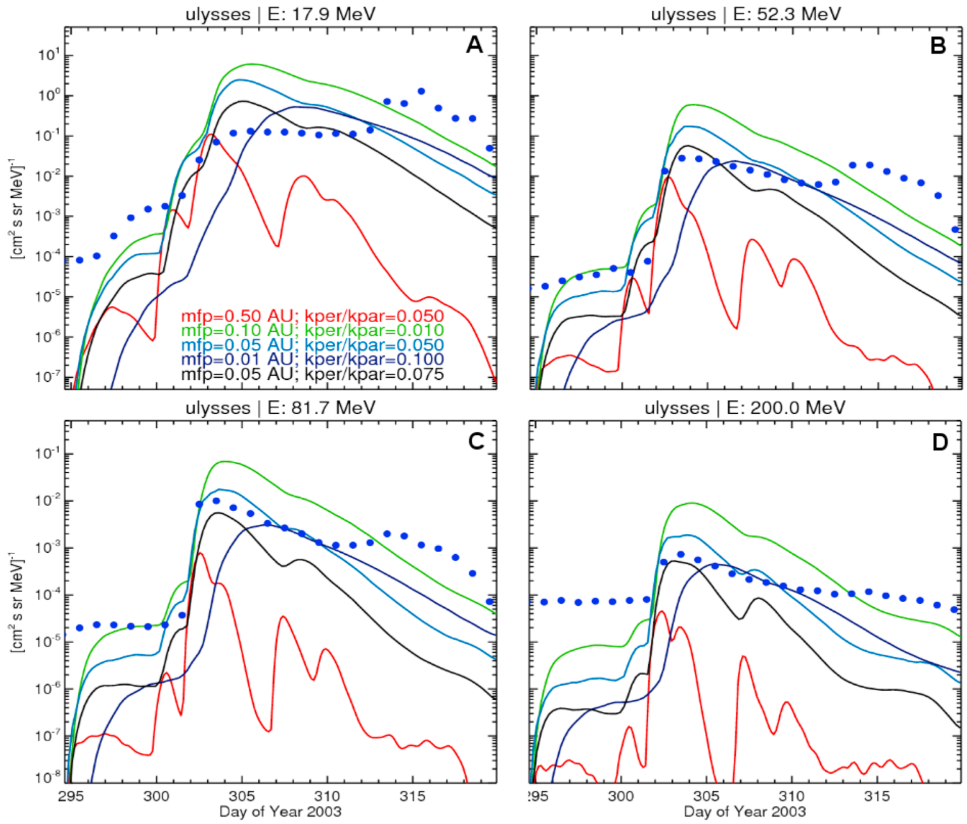

Figure 5. (a–d) Comparison of simulations we have performed in order to determine appropriate transport parameters for the Halloween events. The different color lines correspond to simulations with different combinations of parallel mean free paths and ratios of perpendicular to parallel diffusion coefficients, as described in Figure 5a. The blue solid circles correspond to Ulysses pulse height analysis daily measurements. Figures 5a–5d show flux profiles at 17.9, 52.3, 81.7, and 200.0 MeV.

CME-associated shocks. Such studies would help refine the boundary conditions and the transport parameters of the EPREM model. From running series of simulations, we have determined that there were only big changes to the modeled flux profiles at Ulysses for large parallel mean free paths (bigger than 0.5 AU). Below, we demonstrate obtaining best agreement between modeled and observed fluxes for a particle mean free path of around 0.05 AU. The fluxes outside of the source region are set to zero as an initial condition. The main limitation of this choice of inner boundary for the model is the likely dependence of the SEP profile shapes on longitude, for which we cannot correct presently.

[24] The model was run for a single species, protons, which are the dominant species in SEP events, and thus pose the greatest short-term radiation damage risk. The energy domain for the simulation was 5.0–500.0 MeV. Since the detailed analyses of spacecraft observations by *McKibben et al.* [2005] and *Lario et al.* [2005] have tentatively ruled out the possibility that observed fluxes of protons below 10 MeV around DOY 301 be connected with the corresponding fluxes at Earth temporally, in this work we only present modeled proton fluxes at higher energies. Also, we have attempted to obtain as good a match to particle time series at higher energies (E > 30 MeV) as possible, since those particles may cause the most radiation damage. In order to obtain radial gradients of fluxes and doses that could be used as guidelines for large storms like the Halloween ones, we have strived to get the best overall match to Ulysses data within the capabilities that our model includes.

[25] The simulation solved for the distribution function in four steps in pitch angle. However, since the GOES 11 energetic particle instrument does not record the pitch angle distribution, we have used an isotropic particle distribution as input. To test the effect this assumption might have on the modeled fluxes, we ran two simulations, the only difference between which was the pitch angle distribution of the source at 1 AU. In the first simulation, we used the original data from GOES 11 spread out over four pitch angle steps (μ = −1, −0.33, 0.33, 1), forming an isotropic source distribution. Here, μ is the

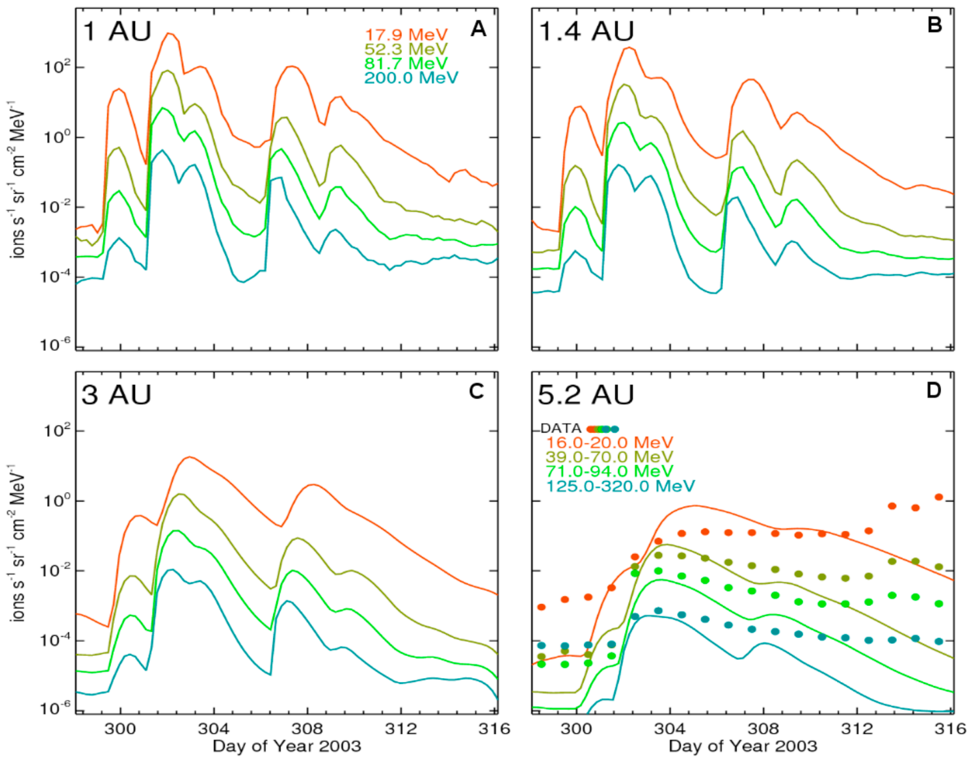

Figure 6. Comparing the simulated energetic proton fluxes as a function of heliospheric distance using time-independent solar wind conditions reveals the gradual merging of individual abrupt enhancements at 1 AU into a single long-duration feature at 5 AU. Energetic particle fluxes at four different locations in the inner heliosphere from the EPREM simulation with analytic solar wind description. Shown are fluxes at (a) Earth (1 AU; heliocentric longitude changes between 315.6° and 332.5°), (b) Mars (1.4 AU; longitude between 295.3° and 305.7°), (c) 3 AU (longitude between 224.4° and 194.9°), and (d) Ulysses (5.2 AU; longitude between 79.9° and 80.1°). Different colors denote fluxes at corresponding energies. Figure 6d shows daily Ulysses COSPIN pulse height analysis proton fluxes, shown as solid circles overplotted on the simulations.

cosine of the proton pitch angle. For the second simulation, we formed a beam distribution by putting the observed distribution function values into the μ = 1 step, and setting the values for the other steps to zero. Both runs were performed with the same scattering mean free path, 0.05 AU. Inspection of the model output at 5.2 AU shows that the average ratio of the first-order anisotropies (used as defined by *Zhang et al.* [2009], and combining the μ = −0.33 and μ = 0.33 to obtain the 90° distribution values) is 1.007 with a standard deviation of 0.06, and the omnidirectional fluxes differ by less than 15%, on average. This difference in omnidirectional fluxes introduces a maximum uncertainty of 15% to our results, but the only change to the profiles is a decrease of the proton levels when using a beam source distribution. Most likely, the distribution is somewhere between these two cases, and closer to an isotropic distribution, so the uncertainty may be reduced to less than 10%.

[26] We have performed a set of simulations in order to determine appropriate values for the two main free parameters of the transport, the particle parallel mean free path, λ_o and the fractional amount of perpendicular transport in terms of the parallel diffusion, $\kappa_{perp}/\kappa_{par}$. Figure 5 shows a comparison at four energies (17.9, 52.3, 81.7, and 200.0 MeV for Figures 5a, 5b, 5c, and 5d) of the EPREM output at 5.2 AU (near Ulysses), for five separate simulations, in which only the mean free path and perpendicular diffusion were varied. The colorful lines correspond to proton flux profiles for the five different combinations of λ_o and $\kappa_{perp}/\kappa_{par}$ values listed in Figure 5a. The blue dots are daily PHA values from Ulysses observations. Figures 5a–5d show the omnidirectional modeled proton flux at four different energies, corresponding to the geometric means of Ulysses COSPIN channels. Observational and theoretical studies have shown that perpendicular transport of protons varies between 1 and 10% [*Dröge*, 2000], we have used values in that range. Furthermore, we found that values of the parallel mean free path larger than 0.1 AU give poor agreement to the data, since observed flux profiles are

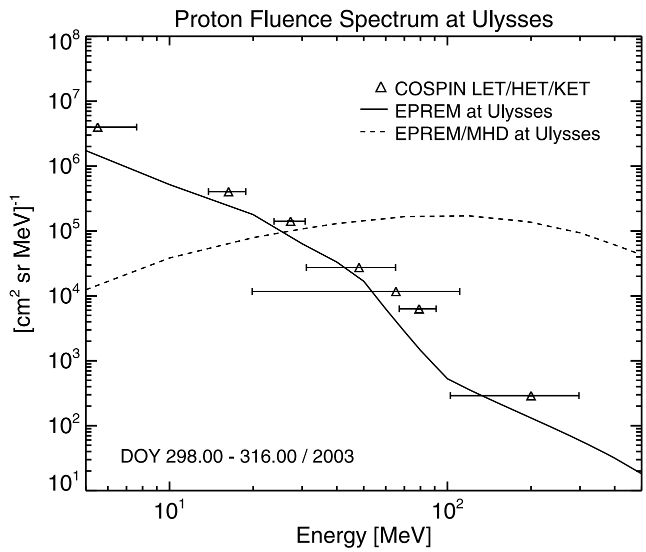

Figure 7. Observed and predicted event-integrated proton fluence spectra at Ulysses. The triangle symbols are observations from the COSPIN [*Simpson et al.*, 1992] instrument suite on Ulysses. The solid line is the fluence spectrum from the EPREM simulation, which agrees quite well with observed fluences. The EPREM +MHD simulation fluences are shown by the dashed line. See section 5 for details of that simulation.

smooth in time, and modeled profiles, such as the red lines in Figure 5 (λ_o = 0.5 AU, $\kappa_{perp}/\kappa_{par}$ = 0.05), show the signatures of 1 AU flux enhancements not seen in Ulysses data. From visual comparison of the modeled profiles with the data, we conclude that the combination λ_o = 0.05 AU, $\kappa_{perp}/\kappa_{par}$ = 0.05 (light blue profile) represents the best agreement in terms of matching the daily averaged data values. In particular, this simulation seems to match best the initial proton flux increases at the energies, at which protons are capable of inflicting radiation damage (Figures 5c and 5d). As mentioned before, we have no hope of matching the secondary increases in the Ulysses data (around DOY 315), since those were caused by the interaction of a corotating stream with a backward halo CME. However, we note the close agreement at energies 81.7 MeV and 200.0 MeV of the peak proton fluxes, which is important for the accumulated radiation doses. We should also note that the high levels of proton fluxes at Ulysses for the two highest energies, and especially at 200.0 MeV, are most likely due to the increased levels GCR fluxes, which EPREM does not consider. Below we discuss more results from this simulation with best agreement to the data.

4.2. Simulation Results

[27] We present simulation results of the simulation with λ_o = 0.05 AU, $\kappa_{perp}/\kappa_{par}$ = 0.05 starting at DOY 298, since it took about 4 days of simulation time for the solution to converge at the outer edge of the computational domain, and for fluxes to accumulate to preevent background levels. Simulated proton fluxes were extracted at the locations of Earth, Mars, Ulysses, and at 3 AU on the nominal spiral line that passes through Ulysses.

[28] Figure 6 shows results from the EPREM simulation, time profiles of simulated fluxes near four different locations, Earth, Mars, 3 AU, and Ulysses (Figures 6a–6d) at four energies. These energies have been chosen to correspond to the geometric mean energies of channels from the COSPIN instrument suite on board Ulysses. The fluxes at these energies were calculated by doing logarithmic interpolation on the energy grid of the EPREM model output. The particle propagation effects can be seen in the comparison of flux enhancements at increasing radial distances from the Sun. The abrupt onsets and rapid decays back to background values that can be seen at 1 AU (Figure 6a) become smoothed out in time, and the magnitude of the flux jumps is also reduced as a function of radial distance, going through Figures 6b–6d. Protons get scattered in pitch angle and in energy, they diffuse along and perpendicular to the nominal Parker spiral field lines. Thus, the five major energetic proton flux enhancements at DOY 299, 301, 306, and 308 on the 1 AU plot (Figure 6a) become merged into a single fast-rise, slow-decay enhancement at 5.2 AU (Figure 6d).

[29] Figure 6d shows the Ulysses/COSPIN daily pulse height analysis (PHA) proton flux values overplotted as solid circles. We predict lower background fluxes than observed before the onset of the event, which we attribute to the fact that EPREM is not treating the boundary conditions for galactic cosmic rays explicitly. Instead, we use the Badhwar-O'Neill model [*O'Neill*, 2006] to calculate the GCR spectra at 1 AU based on solar activity phase (on the value of the solar modulation potential). We then assume flux conservation in order to calculate the spectra at other radial distances from the Sun. Based on these calculated spectra, we compute radiation dose rates for the different locations of interest, and sum them with the doses from the energetic proton fluxes obtained from the EPREM simulations. We have established from our simulations that the GCR contribution to radiation doses for the Halloween events is less than 0.1% for Earth, and less than 10% for Ulysses during the large part of the events.

4.3. Fluxes, Fluences, and Radial Gradients

[30] Figure 7 compares the observed and simulated energetic proton fluence (the time-integrated fluxes over the duration of the events) spectra at Ulysses. The solid and dashed lines denote the fluence spectra from the EPREM and EPREM+Enlil simulations, respectively. Symbols denote Ulysses COSPIN observations. Fluences were calculated by integrating fluxes between DOY 298 and 316. The horizontal bars denote the width of the energy channel on the instruments. For these events we have obtained somewhat good agreement between the observed and simulated fluences. However, the observed fluences are systematically higher than the simulated ones. In our opinion, this is due to the combination of two

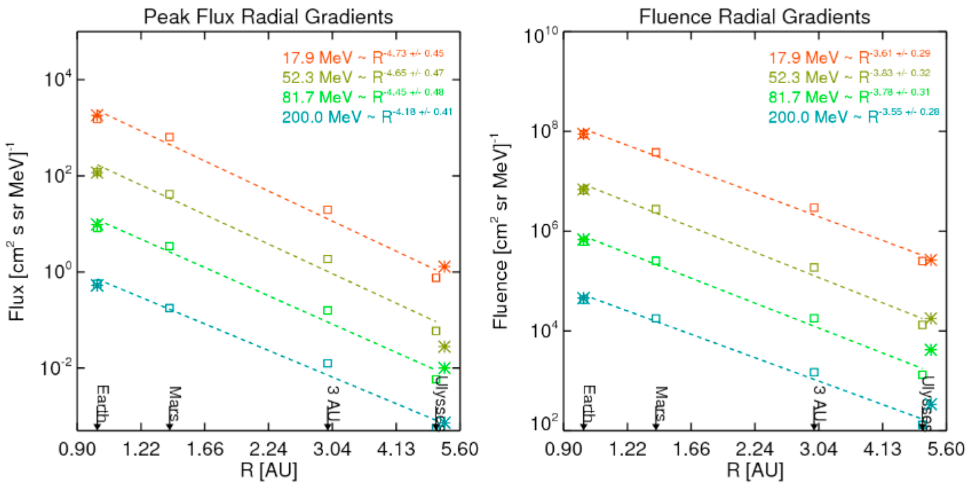

Figure 8. (left) Predicted peak fluxes as a function of radial distance for the EPREM simulation. The points were obtained by finding flux maxima at four locations over the duration of the Halloween events. Dashed lines are power law fits for the dependence of the peak fluxes on radial distance (see text), with power law indices and uncertainties shown in the legend of the plot. The asterisks at 1 AU and 5.2 AU represent measurements from GOES and Ulysses, for comparison. (right) Event-integrated fluences at five energies plotted against radial distance. The dashed lines are power law fits for the dependence of the proton fluences on radial distance, with power law indices and uncertainties shown in the legend of the plot. The asterisks at 1 AU and 5.2 AU represent measurements from GOES and Ulysses, for comparison.

effects: in the lower energies, the added fluence from the secondary increase around DOY 315; in the high end of the spectrum, the contribution of GCRs bumps up the fluences.

[31] Determining radial gradients of particle fluxes and radiation doses is important for characterizing an average overall dependence of the radiation environment on heliocentric distance. Figure 8 (left) shows peak fluxes at four energies as a function of radial distance for the EPREM simulation. Peak fluxes refer to the peaks of the first major enhancement near Earth at DOY 301 and its counterparts at increasing radial distances. The square symbols represent the peak fluxes at the various energies at Earth (318.4° longitude), Mars (297.1°), 3 AU (189.5°; along Ulysses-connected magnetic field line), and near Ulysses (79.3°). The dashed lines are power law fits through the four points (at each energy) of the form

$$J(R) = J_0 (R/R_0)^{\alpha}, \tag{1}$$

where R is the radial distance from the Sun, J_0 is flux at energy E at R_0 = 1 AU, and α is the power law index). The deduced forms of radial dependence are displayed in the legend. Figure 8 (right) shows the simulated proton fluences from the same simulation, integrated over the period studied in this paper. The dependence on radial distance of both peak flux and fluence seems to vary with energy in the EPREM simulation. The slopes of the radial fit to peak fluxes for 81.7 and 200.0 MeV are −4.45 (±0.48) and −4.18 (±0.41), respectively; the corresponding slopes for the event-integrated fluences are −3.78 (±0.31) and −3.55 (±0.28).

4.4. Radial Gradients of Energetic Proton Radiation Doses

[32] We also present gradients in the accumulated Gray equivalent and peak Gray equivalent rates from the EPREM simulation. Dose is a radiometric quantity, equivalent to the energy deposited by incoming radiation in a material or tissue per unit mass (1 Gy = 1 J/1 kg). Gray equivalent is a variation on Dose that is used for determining short-term radiation effects on humans from penetrating protons. It is defined as

$$D(Gy_{eq}) = D(Gy) \times RBE, \tag{2}$$

where RBE is the radial biological effectiveness of the damaging radiation source relative to gamma rays. In the case of SEPs and this study, we have set RBE = 1.5 for protons.

[33] We have chosen to model this quantity, since we would like to characterize the impact SEP protons have, and we look at comparatively short periods of acute radiation. We have used a version of the Baryon Transport (BRYNTRN) code [*Wilson et al.*, 1988] in order to calculate this radiometric quantity for different amounts of aluminum shielding and depths of water. Integration of particle fluxes over all energies is required in order to obtain doses quantities. For the numerical calculations we have instead used a discretized grid of energies ranging between 5 and

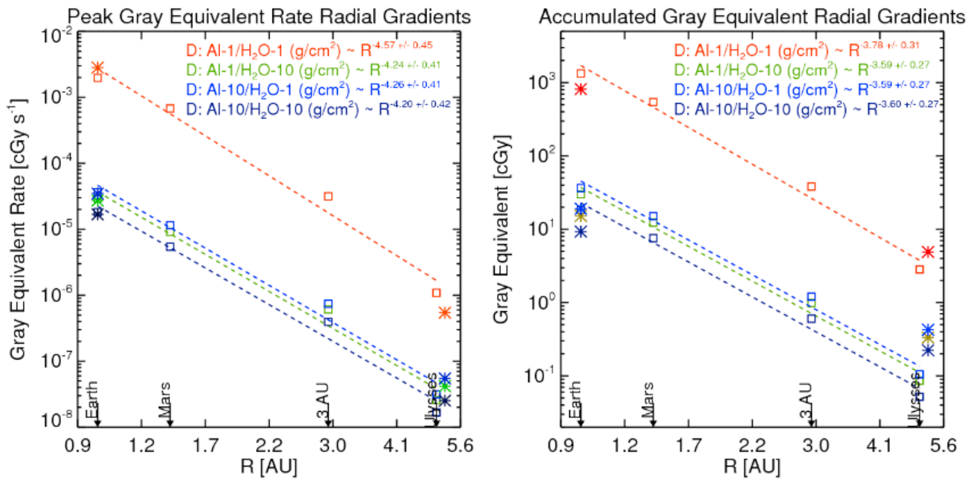

Figure 9. (left) Peak Gray equivalent rates are plotted as a function of radial distance in the heliosphere. They were calculated with the BRYNTRN transport model using predicted fluxes from the EPREM simulation. Different colors correspond to varying thicknesses of aluminum and water (a proxy for human organs). Dashed lines are power law fits for the dependence of the peak Gray equivalents on radial distance, with power indices and uncertainties shown in the legend of the plot. The asterisks at 1 AU and 5.2 AU represent calculations from GOES and Ulysses data for comparison. (right) The modeled dependence of accumulated Gray equivalent values on radial distance shows similar trends as with the peak Gray equivalent rates. The different colors correspond to varying thicknesses of aluminum (thick and thin shielding) and water (representing skin and blood-forming organs). The dashed lines are power law fits for the dependence of the peak Gray equivalents on radial distance, with power indices and uncertainties shown in the legend of the plot. The asterisks at 1 AU and 5.2 AU represent calculations from GOES and Ulysses data for comparison.

2000 MeV, where we have used logarithmic interpolation in energy up to 500 MeV for obtaining fluxes from the EPREM output. For the energies above 500 MeV, we have used least squares fitting to a Weibull spectrum form [*Xapsos et al.*, 2000]. The Weibull spectral profile is widely used in space radiation physics to fit observed proton fluences [*Townsend et al.*, 2003]. Usually, protons below 10 MeV contribute essentially nothing since they cannot penetrate a space suit (their range in aluminum is 0.17 g/cm^2); protons above 700 MeV do not contribute much to the dose either, as they do not impart much of their energy to the material they pass through [*Townsend and Zapp*, 1999]. In order to characterize proton radiation as a function of radial distance from the Sun, we perform the same analysis as we did previously. Figure 9 shows peak Gray equivalent rates and accumulated Gray equivalent through four combinations of aluminum shielding and water as a function of radial distance. Aluminum thickness (column density) of 1 g/cm^2 corresponds approximately to the thickness of a space suit, 10 g/cm^2 is representative of spacecraft shielding. We have used water as a surrogate material to represent skin (1 g/cm^2 thickness), and blood-forming organs (BFO) (10 g/cm^2 thickness). The format is similar to that of Figure 8, with the same type of functional fits through the different material combinations. We find that power law fits with average power law indices of –4.32 (±0.42) and –3.64 (±0.28) describe the decline of peak dose rates and accumulated doses, respectively, for these events. The work by *PourArsalan et al.* [2010] presents more results from the simulations of the radiometric quantities for this event based on EPREM simulations with an analytic solar wind description.

5. Coupling EPREM to Numerical MHD Solar Wind Model Results

5.1. Enlil MHD Heliospheric Model

[34] Enlil is a three-dimensional magnetohydrodynamic code, which solves the ideal MHD equations for a magnetized fluid in spherical coordinates [*Odstrcil*, 2003]. The code ignores microscopic effects, but calculates the global time-dependent behavior of a quasi-neutral, two-fluid, single-temperature plasma. It describes the state of the plasma by its mass density, velocity, pressure, temperature, total energy density, and magnetic field induction. The heliocentric distance of the outer boundary of the Enlil model can be changed depending on the scope of a particular run. The inner boundary surface of the Enlil code is at 20 Rs, or about 0.1 AU. To populate that boundary, Enlil has been coupled to the Wang-Sheeley-Arge (WSA) empirical model [*Arge and Pizzo*, 2000], which

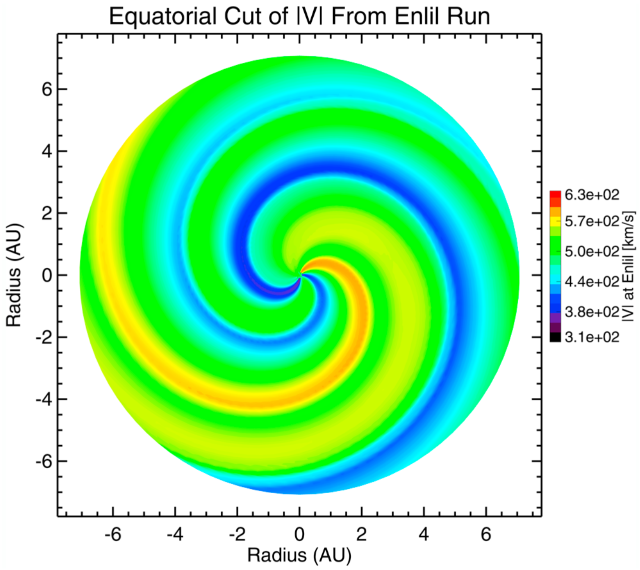

Figure 10. This global view of the simulated solar wind speed in the heliospheric equatorial plane shows complex stream structure with sharp gradients, which may influence significantly particle energetics. The solar wind speed in the inner heliosphere (0.1–7.0 AU) was predicted by the Enlil model, with inputs from photospheric magnetograms and a simulated magnetic configuration of the solar corona from the WSA model.

predicts the solar wind speed at the source surface (0.1 AU) based on photospheric magnetogram observations from an entire rotation of the Sun (Carrington rotation, or CR). The Solar magnetogram for the period including the Halloween events (CR 2009) was obtained from the National Solar Observatory.

[35] A complete 3-D treatment of the heliospheric plasma requires a magnetogram map of the entire Solar surface. The Enlil model produces a single snapshot, a three-dimensional map of the solar wind properties, throughout the heliosphere over one Carrington rotation. Figure 10 shows the time-independent steady state solution for the solar wind speed in the equatorial plane between 0.1 and 7.0 AU during the Halloween events (CR 2009). The recurring interaction regions between fast and slow streams are easily discerned, since the period of the Halloween storms was late in cycle 23, and these streams dominated the heliospheric activity. A time-independent solution for the solar wind conditions in the inner heliosphere is inherently limited in its description of the real solar wind, no matter how good the simulation. This is because it captures the stable streams, CIRs and other structures, but not transient features such as CMEs, which can drive particle-accelerating shocks. Nevertheless, it should still give a more realistic background for the transport of energetic particles than a simple Parker spiral solution. Recent model developments [*Taktakishvili et al.*, 2009] have made it possible to include cone model CMEs into Enlil simulations. Studying SEP events by including such MHD simulations will be undertaken in future work. In this study, we use modeling results from an Enlil simulation, done on request at the Center for Integrated Space Weather Modeling (CISM) at Boston University. That model's computational grid extended radially out to 7 AU, with 937 × 30 × 90 cells in the radial, latitudinal, and azimuthal directions, respectively. The resolution of the Enlil simulation is standard, used for CISM and CCMC simulations and considered sufficient for computational needs such as this application. Computing coefficients of the transport equation requires gradients and time derivatives of MHD parameters in the EPREM domain. We do the coupling between the two codes by performing trilinear interpolation for EPREM nodes on the Enlil grid, so for every node in the EPREM grid we obtain MHD parameters at all time steps. Our simulations suggest that the resolution of the Enlil grid is sufficient for computing the solar wind parameters via this technique.

5.2. Underlying Solar Wind Conditions at Earth and Ulysses

[36] In order to constrain the response of the EPREM model to introduction of dynamical solar wind parameters, we have compared the observed and simulated solar wind magnetic field, density, and speed at 1 AU and Ulysses. Figure 11 shows measurements from the SWEPAM [*McComas et al.*, 1998] and MAG [*Smith et al.*, 1998] instruments on board the ACE spacecraft (asterisks) overplotted on the modeled EPREM+Enlil (solid lines) and EPREM (dashed lines) values. Figure 12 shows a comparison between observations and what the EPREM model used for the solar wind density, speed and magnetic field magnitude time profiles at the position of Ulysses. The observational data (shown with triangles, diamonds and asterisks) were obtained from the SWOOPS [*Bame et al.*, 1992] and VHM [*Balogh et al.*, 1992] instruments. The horizontal dashed lines correspond to solar wind parameters from the EPREM simulation, and the solid lines were obtained by recording the MHD conditions at the Ulysses observer from the EPREM+Enlil simulation. We overplot the passages of interplanetary shocks and ICMEs from *Lario et al.* [2005] for both ACE and Ulysses. The results obtained by including time-dependent MHD parameters show much more dynamic conditions. For these complex events the agreement between observed and predicted MHD parameters was poor. This is likely due to several effects: First, Enlil depends on boundary conditions and do not always agree with observations; Second, we included an MHD map that only includes the nominal Parker spiral and recurrent streams and CIRs. In reality, the Halloween event was very complex, as it featured multiple interplanetary shocks and ICMEs. Including Enlil time-dependent simulations with CME cone models into EMMREM modeling is the scope of future work. Finally, the com-

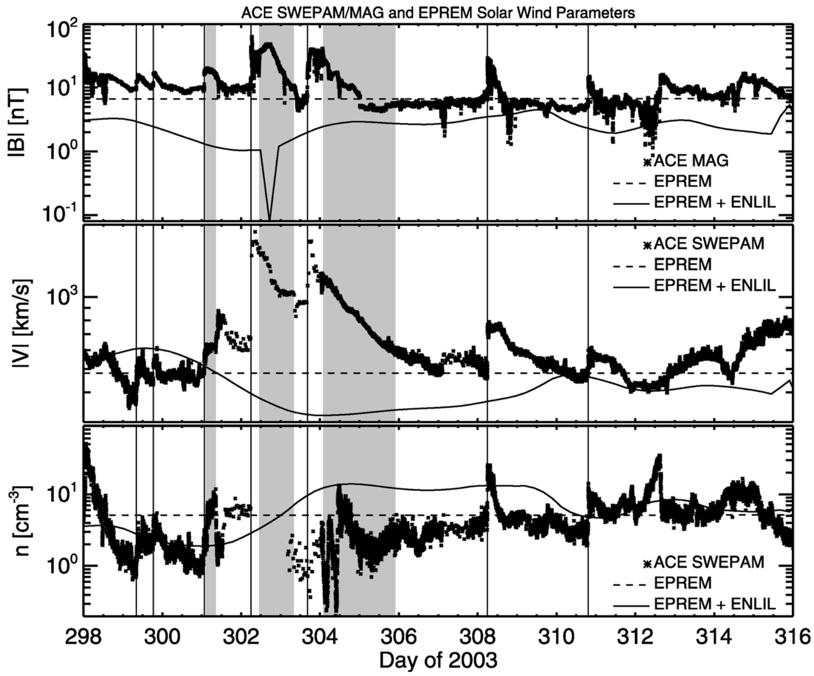

Figure 11. The real conditions of the inner heliosphere captured by observations prove to be even more complicated and dynamic than simulations predict, and there is often significant mismatch. Shown are the observed and modeled (steady state) solar wind parameters time history at L1 (ACE spacecraft) during the Halloween events. The symbols show observations from the MAG [*Smith et al.*, 1998] and SWEPAM [*McComas et al.*, 1998] instruments onboard ACE. The solid lines show the predicted solar wind parameters at L1 within the EPREM+ENLIL simulation. The dashed line represents the solar wind parameters at the same location from the EPREM simulation with analytic SW parameters. CME passages are denoted as gray-shaded regions, and interplanetary shocks are denoted as vertical solid lines.

putational grid of EPREM is dynamic, and the positions of a given node depends on the solar wind values in the vicinity of that node.

5.3. Comparison of EPREM and EPREM+Enlil Simulations With Ulysses Observations

[37] Figure 13 shows a comparison between Ulysses-observed fluxes at the four energies we have used throughout the paper (blue solid circles), and three simulations. The smooth blue lines correspond to the EPREM simulation discussed in section 4.2, while the green and red lines correspond to two simulations in which we have coupled EPREM to results from the Enlil MHD simulation for that Carrington rotation. Overall, the agreement of the two EPREM+Enlil simulations with Ulysses data is poor. Fluxes do not decline significantly with energy, leading to a much harder spectrum than observed (dashed line in Figure 7). Unlike the EPREM simulations, in the EPREM+Enlil simulations fluxes do not seem to be affected much by varying the scattering mean free path and the amount of perpendicular diffusion, judging from the two simulations in Figure 13. This will be further investigated. However, a possible correlation of the flux increase is seen around DOY 314 between modeled and observed profiles, which might correspond to particle acceleration caused by the arrival of a CIR. A corotating stream was reported to reach Ulysses at that time (albeit in combination with a fast CME), and it is possible that large plasma gradients in its modeled counterpart within Enlil have caused local acceleration of protons. The CIR is visible in all three panels of Figure 12, between DOY 311 and 314.

[38] Overall, the coupling between our particle model and MHD solar wind models would benefit from better modeling results from the numerical MHD modeling at farther radial distances. We hope to improve the coupling and investigate the possible applications of the coupled models.

6. Summary

[39] We present a modeling study of energetic proton propagation and corresponding radiation effectiveness during the 2003 Halloween events. The results from this study show that EPREM predictions match the observed fluxes from the energetic particle instrument suite COSPIN on the Ulysses spacecraft reasonably well (for a suitable combination of prescribed scattering mean

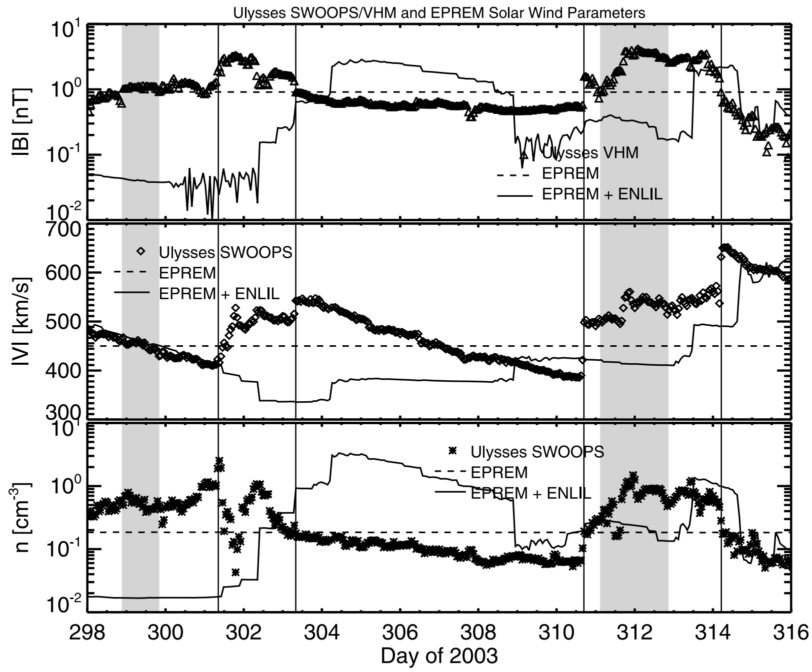

Figure 12. The simulated steady state solar wind at 5.2 AU reveals sharp gradients in the MHD parameters, but observations show more gradual changes of the solar wind conditions. A plot of the observed and modeled solar wind parameters time history at the location of Ulysses during the Halloween events. The symbols show observations from the Vector Helium Magnetometer (VHM) [*Balogh et al.*, 1992] and Solar Wind Observations Over the Poles of the Sun (SWOOPS) [*Bame et al.*, 1992] instruments onboard Ulysses. The solid lines show the predicted solar wind parameters at the location of Ulysses within the EPREM/ENLIL simulation. The dashed line represents the solar wind parameters at the same location from the EPREM simulation with analytic SW parameters. CME passages are denoted as gray-shaded regions, and interplanetary shocks are denoted as vertical solid lines.

free path of 0.05 AU and perpendicular diffusion coefficient that is 5% of the parallel one), and give us confidence in the model's performance. By obtaining such an agreement to data at 5.2 AU, we can use model results to obtain simulated radial gradients of fluxes, fluences, and dose quantities in the inner heliosphere. These results could be of potential value to mission planners and radiation physics researchers.

[40] The first simulation we present (Figure 6) includes an analytic description of the solar wind parameters based on magnetic and mass flux conservation. We performed a series of simulations, in order to determine the transport parameters that give closest agreement to observations during the Halloween storms. We have attempted to match the initial onset time of the storms at Ulysses, as well as the primary peak, which was associated with the event with hardest spectra near Earth. Since we are interested in the application of our model to characterizing particle radiation, we have attempted to obtain best agreement between time series at relevant energies (E > 30 MeV). The model does not capture a secondary increase in proton fluxes, which was caused by the interaction of a fast backward halo CME and a CIR. From the results of this simulation, we determine radial gradients of peak fluxes, event integrated fluences, radiation dose rates and accumulated doses. We fit power law relationships for four locations between 1 and 5.2 AU, for which we have model output. For peak fluxes and event-integrated fluences at 200 MeV, we obtain power indices of −4.18 and −3.55, which show steeper decline than what is usually reported [*Dayeh et al.*, 2010]. For the radial gradients of proton peak dose rates and accumulated doses, we find average power law indices of −4.32 and −3.64, similar to the radial gradients of peak flux and fluence.

[41] In an attempt to obtain more accurate characterization of the solar wind environment in the inner heliosphere for SEP propagation modeling for these events, we have used results from three-dimensional modeling of the solar wind conditions with the WSA/Enlil heliospheric model. We find that the simulated proton fluxes with the coupled EPREM+Enlil model have responded to the gradients in the underlying time-dependent MHD parameters for the solar wind, but the agreement to observed Ulysses fluxes is poor overall. That we attribute to the poor

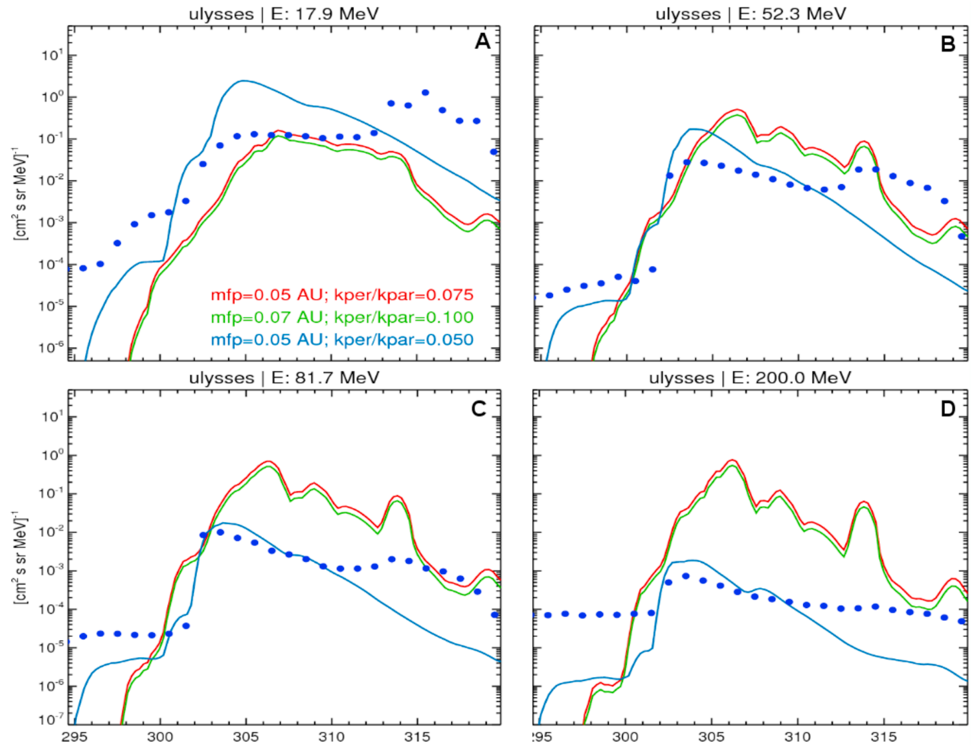

Figure 13. (a–d) Comparison of proton flux simulations and observations during the Halloween events. The blue lines are results from the EPREM simulation that was determined to best match Ulysses data at 81.7 and 200.0 MeV, and the red and green lines are proton fluxes from two simulations which included numerical MHD modeling of the solar wind conditions in the heliosphere. The transport parameter combinations are described in Figure 13a. The blue solid circles correspond to Ulysses pulse height analysis daily measurements. Figures 13a–13d show flux profiles at 17.9, 52.3, 81.7, and 200.0 MeV.

agreement between the simulated and observed solar wind parameters at 5.2 AU. We were able to achieve a single correlation between modeled and observed flux enhancements near Ulysses, associated with a CIR passage by the spacecraft location, that we would not have been able to predict without the inclusion of the dynamic solar wind model. Overall, improved MHD simulation results are required in order to be able to characterize more accurately the interplanetary radiation environment beyond 1 AU, as SW parameters influence the energetic particles fluxes significantly. One such effort is the undergoing development of a global heliospheric MHD code at Boston University. We are concurrently developing an interface between EPREM and this model, and hope to improve EPREM's predictions as a result of using its predictions for the solar wind.

[42] There is further room for improvements to the EMMREM framework. Currently, several of its most important features are in place, and in use, the EPREM module, the interface to numerical MHD global heliospheric models, as well as the interface to codes that calculate secondary particle transport and radiation quantities. Improved knowledge about the angular extent of events would be necessary to constrain the definition of EPREM's boundary conditions. Future studies involving multispacecraft observations, including the STEREO mission [*Kaiser et al.*, 2008], may be a great aid in this area. We still have to address the important question of particle acceleration at traveling shocks. We will use results from the Particle Acceleration in The Heliosphere (PATH) model [*Verkhoglyadova et al.*, 2008], in order to incorporate fluxes of shock-accelerated energetic particles into the predictions of the EMMREM framework for future studies. We have shown the first results of coupling between the 3-D EPREM energetic particle model and results of MHD simulations. This represents a significant step in our ability to specify the energetic particle environment of our inner heliosphere as it changes in response to large-scale disturbances such as coronal mass ejections and corotating interaction regions.

Appendix A: Computation of Perpendicular Diffusion in EPREM

[43] As noted by *Schwadron et al.* [2010], the EPREM model includes a solution for the effects of diffusion and

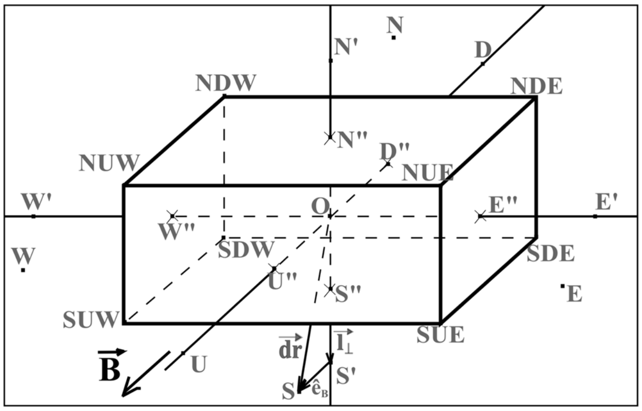

Figure A1. A graphical description of an idealized node interface to neighboring points. The magnetic field vector points in the direction out of the page, $\overrightarrow{OU}$.

drifts of energetic particles perpendicular to the magnetic field at each computational cell. This is done by solving a separate convection-diffusion equation (in addition to solving the focused transport equation) of the form

$$\frac{\partial f_0}{\partial t} = \nabla \cdot \left(\kappa_\perp \cdot \nabla f_0\right) - \mathbf{v}_D \cdot \nabla f_0, \tag{A1}$$

where

$$\mathbf{v}_D = \frac{cvp}{3q} \nabla \times \left(\frac{\mathbf{B}}{B^2}\right). \tag{A2}$$

Considering only the effects of perpendicular diffusion, we obtain

$$\frac{\partial f_0}{\partial t} = \nabla \cdot \left(\kappa_\perp \cdot \nabla f_0\right), \tag{A3}$$

where $\kappa_\perp$ is the perpendicular diffusion coefficient. Integrating both sides of the equation, and using Gauss's theorem, we have

$$\frac{\partial}{\partial t}\int_V f_0 dV = \int_V \nabla \cdot \left(\kappa_\perp \cdot \nabla f_0\right) dV, \tag{A4}$$

$$\frac{\partial}{\partial t}\int_V f_0 dV = \oint_\mathbf{A} \left(\kappa_\perp \cdot \nabla f_0\right) \cdot d\mathbf{A}, \tag{A5}$$

$$V\frac{\partial f_0}{\partial t} = \oint_\mathbf{A} \left(\kappa_\perp \cdot \nabla f_0\right) \cdot d\mathbf{A}. \tag{A6}$$

The left-hand side gives the volume of the enclosed surface, multiplied by the time change of the average distribution function.

[44] In order to calculate this change on the computational grid, we find for every computational node six neighboring nodes, the distance to which is found at every time step. Two of the nodes are on the same field line as the original node, one inward and one outward of it. The other four, which we will call "perpendicular," are corresponding nodes on two-by-two neighboring field lines in longitude and latitude (we will also use "node" and "point" interchangeably, referring to the computational grid structure). We designate the perpendicular nodes North, East, West, and South (commonly abbreviated as *NEWS* in the rest of this appendix); the neighboring node inward to a given node on their shared magnetic field line (also called a streamline here) is referred to as the Down neighbor (abbreviated as *D*), and the one outward is called the Up neighbor (*U*). Figure A1 shows the interface between a given node, denoted as point *O*, and the NEWS neighbors, as well as the Up and Down nodes on the same magnetic field line. We use a triple-point second-order-accurate finite differencing conservative scheme to solve for the perpendicular gradient of the distribution function, by discretizing it in four directions to these neighboring points. Equation (A6) is discretized as

$$\triangle f_0 = \frac{\triangle t}{V}\sum_{i=1}^{6} \kappa_\perp \left(\nabla f_0\right)_i A_i, \tag{A7}$$

where V is the volume enclosed by the six neighbor areas defined below, and the index i goes over every such area.

[45] The area elements are constructed as follows. For every NEWS neighbor of a given node, we find the projection of the distance between it and the node perpendicular to the magnetic field direction at the node, $\hat{\mathbf{e}}_\mathbf{b} = \frac{\mathbf{B}(O)}{|\mathbf{B}(O)|}$. In Figure A1 this corresponds to the distances ON', OE', OW', OS'. The midpoints of these distances are the third points used for calculating the gradient of f_0 in that direction; these are points N'', E'', W'', S''. The volume V is constructed from the intersection of planes constructed through these midpoints parallel to the magnetic field direction at node O, as well as through the midpoints (U'', D'') of the distances to the two U, D neighbor points (The last two planes are perpendicular to the magnetic field direction). Since the normals of the areas through points U'', D'' are in a direction parallel to the magnetic field, there is no contribution to the perpendicular diffusion of f_0, and we do not include them in the calculation of the cross-field diffusion.

[46] The perpendicular distances define vectors $\mathbf{l}_\perp$ for each neighboring point. This is shown in the bottom of Figure A1 and more clearly in Figure A2. The vector $\mathbf{dr}$ corresponds to the difference between the position of the central node and its neighbor. Then

$$\mathbf{l}_\perp = \mathbf{dr} - (\mathbf{dr}\cdot\hat{\mathbf{e}}_\mathbf{b})\hat{\mathbf{e}}_\mathbf{b}. \tag{A8}$$

[47] The gradient of f_0 in the perpendicular directions is then given by

$$\left(\nabla f_0(O)\right)_\perp = \sum_i^{NEWS} \frac{f_0(i) - f_0(O)}{|\mathbf{l}_\perp(i)|}, \tag{A9}$$

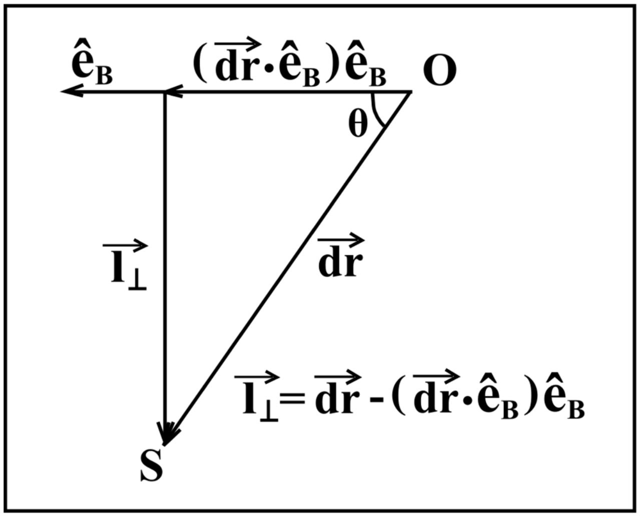

Figure A2. An illustration of the computation of the perpendicular projection of the distance to neighboring points to a given node *O*. The projection of **dr** perpendicular to the direction of the magnetic field ($\hat{\mathbf{e}}_b$) at *O* is $\mathbf{l}_\perp$. It is used in computing the perpendicular gradient of f_0.

where the sum is over all *NEWS* neighboring points, $f_0(i)$ denotes the value of f_0 at each of the neighboring points, and $f_0(O)$ is the value at the node *O*, at a particular time of the simulation.

[48] The perpendicular diffusion coefficient depends on the particle energy via their velocity and mean free path, and this has been included in the numerical scheme. The cross-field diffusion time step, Δt is divided into a number of computational substeps. The substeps are determined by calculating the smallest timescale for perpendicular transport to the neighboring points: $\Delta t = \frac{1}{4}\frac{l_\perp^2}{\kappa_\perp}$. Finding the smallest computational substep ensures the numerical stability of this explicit computational method.

[49] **Acknowledgments.** K.K. would like to thank Sarah McGregor for the helpful discussions regarding Enlil and for running the WSA/Enlil simulations at CISM/Boston University. Research support from the NASA LWS EMMREM project and grant NNX07AC14G is gratefully acknowledged.

References

Aran, A., D. Lario, B. Sanahuja, R. G. Marsden, M. Dryer, C. D. Fry, and S. M. P. McKenna-Lawlor (2007), Modeling and forecasting solar energetic particle events at Mars: The event on 6 March 1989, *Astron. Astrophys.*, *469*, 1123–1134, doi:10.1051/0004-6361:20077233.

Arge, C. N., and V. J. Pizzo (2000), Improvement in the prediction of solar wind conditions using near-real time solar magnetic field updates, *J. Geophys. Res.*, *105*, 10,465–10,480, doi:10.1029/1999JA900262.

Baker, D. N., et al. (2009), Space environment of Mercury at the time of the first MESSENGER flyby: Solar wind and interplanetary magnetic field modeling of upstream conditions, *J. Geophys. Res.*, *114*, A10101, doi:10.1029/2009JA014287.

Balogh, A., T. J. Beek, R. J. Forsyth, P. C. Hedgecock, R. J. Marquedant, E. J. Smith, D. J. Southwood, and B. T. Tsurutani (1992), The magnetic field investigation on the Ulysses mission: Instrumentation and preliminary scientific results, *Astron. Astrophys. Suppl. Ser.*, *92*, 221–236.

Bame, S. J., D. J. McComas, B. L. Barraclough, J. L. Phillips, K. J. Sofaly, J. C. Chavez, B. E. Goldstein, and R. K. Sakurai (1992), The Ulysses solar wind plasma experiment, *Astron. Astrophys. Suppl. Ser.*, *92*, 237–265.

Cane, H. V., D. V. Reames, and T. T. von Rosenvinge (1988), The role of interplanetary shocks in the longitude distribution of solar energetic particles, *J. Geophys. Res.*, *93*, 9555–9567, doi:10.1029/JA093iA09p09555.

Cucinotta, F. A., W. Schimmerling, J. W. Wilson, L. E. Peterson, G. D. Badhwar, P. B. Saganti, and J. F. Dicello (2001), Space radiation cancer risks and uncertainties for Mars missions, *Radiat. Res.*, *156*, 682–688.

Dayeh, M. A., M. I. Desai, K. Kozarev, N. A. Schwadron, L. W. Townsend, M. PourArsalan, C. Zeitlin, and R. B. Hatcher (2010), Modeling proton intensity gradients and radiation dose equivalents in the inner heliosphere using EMMREM: May 2003 solar events, *Space Weather*, doi:10.1029/2009SW000566, in press.

Dröge, W. (2000), Particle scattering by magnetic fields, *Space Sci. Rev.*, *93*, 121–151, doi:10.1023/A:1026588210726.

Dryer, M., Z. Smith, C. D. Fry, W. Sun, C. S. Deehr, and S.-I. Akasofu (2004), Real-time shock arrival predictions during the "Halloween 2003 epoch," *Space Weather*, *2*, S09001, doi:10.1029/2004SW000087.

Dwyer, J. R., G. M. Mason, J. E. Mazur, J. R. Jokipii, T. T. von Rosenvinge, and R. P. Lepping (1997), Perpendicular transport of low-energy corotating interaction region-associated nuclei, *Astrophys. J.*, *490*, L115–L118, doi:10.1086/311003.

Giacalone, J. (1998), Cosmic-ray transport coefficients, *Space Sci. Rev.*, *83*, 351–363.

Kaiser, M. L., T. A. Kucera, J. M. Davila, O. C. St. Cyr, M. Guhathakurta, and E. Christian (2008), The STEREO mission: An introduction, *Space Sci. Rev.*, *136*, 5–16, doi:10.1007/s11214-007-9277-0.

Kallenrode, M.-B. (2001), Shock as a black box: 2. Effects of adiabatic deceleration and convection included, *J. Geophys. Res.*, *106*, 24,989–25,004, doi:10.1029/2001JA900083.

Kallenrode, M.-B., and G. Wibberenz (1997), Propagation of particles injected from interplanetary shocks: A black box model and its consequences for acceleration theory and data interpretation, *J. Geophys. Res.*, *102*, 22,311–22,334, doi:10.1029/97JA01677.

Kallenrode, M.-B., G. Wibberenz, H. Kunow, R. Müller-Mellin, V. Stolpovskii, and N. Kontor (1993), Multi-spacecraft observations of particle events and interplanetary shocks during November/December 1982, *Sol. Phys.*, *147*, 377–410, doi:10.1007/BF00690726.

Kocharov, L., V. J. Pizzo, D. Odstrcil, and R. D. Zwickl (2009), A unified model of solar energetic particle transport in structured solar wind, *J. Geophys. Res.*, *114*, A05102, doi:10.1029/2008JA013837.

Kóta, J., W. B. Manchester, J. R. Jokipii, D. L. de Zeeuw, and T. I. Gombosi (2005), Simulation of SEP acceleration and transport at CME-driven shocks, in *The Physics of Collisionless Shocks: 4th Annual IGPP International Astrophysics Conference*, edited by G. Li, Zank, and Russell, *AIP Conf. Proc.*, *781*, 201–206, doi:10.1063/1.2032697.

Lario, D., R. B. Decker, S. Livi, S. M. Krimigis, E. C. Roelof, C. T. Russell, and C. D. Fry (2005), Heliospheric energetic particle observations during the October–November 2003 events, *J. Geophys. Res.*, *110*, A09S11, doi:10.1029/2004JA010940.

Mason, G. M., et al. (1999), Origin, injection, and acceleration of CIR particles: Observations report of Working Group 6, *Space Sci. Rev.*, *89*, 327–367, doi:10.1023/A:1005278214143.

McComas, D. J., S. J. Bame, P. Barker, W. C. Feldman, J. L. Phillips, P. Riley, and J. W. Griffee (1998), Solar Wind Electron Proton Alpha Monitor (SWEPAM) for the Advanced Composition Explorer, *Space Sci. Rev.*, *86*, 563–612, doi:10.1023/A:1005040232597.

McKibben, R. B., J. D. Anglin, J. J. Connell, S. Dalla, B. Heber, H. Kunow, C. Lopate, R. G. Marsden, T. R. Sanderson, and M. Zhang (2005), Energetic particle observations from the Ulysses COSPIN instruments obtained during the October–November 2003 events, *J. Geophys. Res.*, *110*, A09S19, doi:10.1029/2005JA011049.

Neal, J. S., T. F. Nichols, and L. W. Townsend (2008), Importance of predicting the dose temporal profile for large solar energetic particle events, *Space Weather*, *6*, S09004, doi:10.1029/2008SW000393.

Odstrcil, D. (2003), Modeling 3-D solar wind structure, *Adv. Space Res.*, *32*, 497–506, doi:10.1016/S0273-1177(03)00332-6.

O'Neill, P. M. (2006), Badhwar-O'Neill galactic cosmic ray model update based on Advanced Composition Explorer (ACE) energy spectra from 1997 to present, *Adv. Space Res.*, *37*, 1727–1733, doi:10.1016/j.asr.2005.02.001.
PourArsalan, M., L. W. Townsend, N. A. Schwadron, K. Kozarev, M. A. Dayeh, and M. I. Desai (2010), Time-dependent estimates of organ dose and dose equivalent rates for human crews in deep space from the 26 October 2003 solar energetic particle event (Halloween event) using the Earth-Moon-Mars Radiation Environment Module, *Space Weather*, *8*, S00E05, doi:10.1029/2009SW000533.
Reames, D. V. (1999), Particle acceleration at the Sun and in the heliosphere, *Space Sci. Rev.*, *90*, 413–491, doi:10.1023/A:1005105831781.
Roelof, E. C. (1969), Propagation of solar cosmic rays in the interplanetary magnetic field, in *Lectures in High-Energy Astrophysics*, edited by H. Ögelman and J. R. Wayland, *NASA Spec. Publ.*, *SP-199*, 111–135.
Ruffolo, D. (1995), Effect of adiabatic deceleration on the focused transport of solar cosmic rays, *Astrophys. J.*, *442*, 861–874, doi:10.1086/175489.
Ruzmaikin, A., G. Li, G. Zank, J. Feynman, and I. Jun (2005), The radial dependence of solar energetic particle fluxes, in *"Connecting Sun and Heliosphere": Proceedings of Solar Wind 11/SOHO 16*, edited by B. Fleck and T. H. Zurbuchen, *Eur. Space Agency Spec. Publ.*, *ESA SP592*, 441–444.
Sauer, H. H. (1993), GOES observations of energetic protons to $E >$ 685 MeV: Description and data comparison, *Proc. Int. Conf. Cosmic Rays 23rd*, *3*, 250–253.
Schwadron, N. A., et al. (2010), Earth-Moon-Mars Radiation Environment Module framework, *Space Weather*, *8*, S00E02, doi:10.1029/2009SW000523.
Simpson, J. A., et al. (1992), The Ulysses cosmic ray and solar particle investigation, *Astron. Astrophys. Suppl. Ser.*, *92*, 365–399.
Smith, C. W., J. L'Heureux, N. F. Ness, M. H. Acuña, L. F. Burlaga, and J. Scheifele (1998), The ACE magnetic fields experiment, *Space Sci. Rev.*, *86*, 613–632, doi:10.1023/A:1005092216668.
Taktakishvili, A., M. Kuznetsova, P. MacNeice, M. Hesse, L. Rastätter, A. Pulkkinen, A. Chulaki, and D. Odstrcil (2009), Validation of the coronal mass ejection predictions at the Earth orbit estimated by ENLIL heliosphere cone model, *Space Weather*, *7*, S03004, doi:10.1029/2008SW000448.
Townsend, L. W., and E. N. Zapp (1999), Dose uncertainties for large solar particle events: Input spectra variability and human geometry approximations, *Radiat. Meas.*, *30*, 337–343.
Townsend, L. W., E. N. Zapp, D. L. Stephens, and J. L. Hoff (2003), Carrington flare of 1859 as a prototypical worst-case solar energetic particle event, *IEEE Trans. Nucl. Sci.*, *50*, 2307–2309, doi:10.1109/TNS.2003.821602.
Verkhoglyadova, O. P., G. Li, G. P. Zank, and Q. Hu (2008), Modeling a mixed SEP event with the PATH model: December 13, 2006, in *Particle Acceleration and Transport in the Heliosphere and Beyond: 7th Annual International Astrophysics Conference*, edited by G. Li et al., *AIP Conf. Proc.*, *1039*, 214–219, doi:10.1063/1.2982448.
Webb, D. F., et al. (2009), Study of CME propagation in the inner heliosphere: SOHO LASCO, SMEI and STEREO HI observations of the January 2007 events, *Sol. Phys.*, *256*, 239–267, doi:10.1007/s11207-009-9351-8.
Wilson, J. W., L. W. Townsend, S. Y. Chun, W. W. Buck, F. Khan, and F. Cucinotta (1988), BRYNTRN: A baryon transport computer code—Computation procedures and data base, *NASA Tech. Memo.*, *NASA TM-4037*, 42 pp.
Wilson, J. W., et al. (1991), Transport methods and interactions for space radiations, *NASA Ref. Publ.*, *RP 1257*, 615 pp.
Xapsos, M. A., J. L. Barth, E. G. Stassinopoulos, S. R. Messenger, R. J. Walters, G. P. Summers, and E. A. Burke (2000), Characterizing solar proton energy spectra for radiation effects applications, *IEEE Trans. Nucl. Sci.*, *47*, 2218–2223, doi:10.1109/23.903756.
Zank, G. P., W. K. M. Rice, and C. C. Wu (2000), Particle acceleration and coronal mass ejection driven shocks: A theoretical model, *J. Geophys. Res.*, *105*, 25,079–25,096, doi:10.1029/1999JA000455.
Zhang, M., G. Qin, and H. Rassoul (2009), Propagation of solar energetic particles in three-dimensional interplanetary magnetic fields, *Astrophys. J.*, *692*, 109–132, doi:10.1088/0004-637X/692/1/109.

M. A. Dayeh and M. I. Desai, Southwest Research Institute, 6220 Culebra Rd., San Antonio, TX 78238-5166, USA. (maldayeh@swri.edu; mdesai@swri.edu)

K. Kozarev and N. A. Schwadron, Department of Astronomy, Boston University, 725 Commonwealth Ave., Boston, MA 01760, USA. (kamen@bu.edu; nathanas@bu.edu)

M. PourArsalan and L. W. Townsend, Department of Nuclear Engineering, University of Tennessee, 211 Pasqua Nuclear Engineering Bldg., 1004 Estabrook Rd., Knoxville, TN 37996-2300, USA. (mpourars@utk.edu; ltownsen@tennessee.edu)